

## Highlights

### **Effect of elevated pressure on air-assisted primary atomization of coaxial liquid jets: basic research for entrained flow gasification**

Zhang, Feichi, Zirwes, Thorsten, Müller, Thomas, Wachter, Simon, Jakobs, Tobias, Habisreuther, Peter, Zarzalis, Nikolaos, Trimis, Dimosthenis, Kolb, Thomas

- Simulations of primary breakup process of high-viscous liquid jet at elevated pressures
- Detailed resolution of near-field multiphase interactions for elucidating the breakup mechanism
- Effect of elevated pressure is equivalent to that of increased momentum flux ratio
- Strongly enhanced multiphase momentum exchange at elevated pressure
- First-order estimate proposed for assessing spray dynamics/droplet-velocity

# Effect of elevated pressure on air-assisted primary atomization of coaxial liquid jets: basic research for entrained flow gasification

Zhang, Feichi<sup>a,\*</sup>, Zirwes, Thorsten<sup>a,b</sup>, Müller, Thomas<sup>a</sup>, Wachter, Simon<sup>c</sup>, Jakobs, Tobias<sup>c</sup>, Habisreuther, Peter<sup>a</sup>, Zarzalis, Nikolaos<sup>a</sup>, Trimis, Dimosthenis<sup>a</sup> and Kolb, Thomas<sup>c</sup>

<sup>a</sup>Engler-Bunte-Institute, Division of Combustion Technology, Karlsruhe Institute of Technology, Engler-Bunte-Ring 1, 76131 Karlsruhe, Germany

<sup>b</sup>Steinbuch Centre for Computing (SCC), SimLab Energy & Competence Centre ING, Karlsruhe Institute of Technology, Hermann-von-Helmholtz-Platz 1, Karlsruhe, Germany

<sup>c</sup>Institute for Technical Chemistry, Karlsruhe Institute of Technology, Herrmann-von-Helmholtz-Platz 1, 76344 Eggenstein-Leopoldshafen, Germany

---

## ARTICLE INFO

### Keywords:

Entrained Flow Gasification  
Air-Assisted Atomization  
Primary Breakup  
Elevated Pressure  
Volume of Fluid (VOF)  
OpenFOAM

---


## ABSTRACT

Highly resolved numerical simulations have been conducted for a generic, coaxial air-blast atomizer designed for fundamental research of entrained flow gasification processes. Objective of the work is to gain a detailed knowledge of the influence of elevated reactor pressure on the primary atomization behaviour of high-viscous liquid jets. In agreement with measured breakup morphology and breakup regimes proposed in literature, the simulations yield a pulsating mode instability of liquid jet, along with disintegrations of fibre-type liquid fragments for different pressures. From the mechanism point of view, the breakup process has been shown to be triggered by concentric, axisymmetric ring vortices, which disturb the liquid jet surface in a first stage and penetrate further into the intact core, leading to interfacial instabilities and pinch-off of liquid ligaments. The liquid jet breaks up faster at elevated pressure, leading to a shorter core length  $L_C$ . The calculated exponent ( $b \approx -0.5$ ) of the power law for fitting the decrease of  $L_C$  with  $p$  agrees well with measured correlations from literature in terms of varied momentum flux ratio  $M$  and Weber number  $We_G$ , although water jets, atmospheric pressure and different air-assisted, external mixing nozzles were used in these works. Therefore, the effect of elevated pressure is equivalent to that of increased  $M$  or  $We_G$ , which scale linearly with  $p$  or the gas density for the current setup. The specific kinetic energy of liquid  $k_L$  has been found to be increased with  $p$ , which is particularly pronounced in the high frequency range. A first-order estimate has been proposed, which can be used for the evaluation of liquid kinetic energy or droplet velocity within the spray. The results have been validated by simulations with twice-refined resolution, yielding a grid-independence behaviour with respect to the primary breakup characteristics. However, the follow-up processes with secondary breakup and spray dispersion are reproduced better by using the finer grid.

---

Word Count: 7100

\*Corresponding author

 feichi.zhang@kit.edu (Z. Feichi)

ORCID(s): 0000-0003-3260-5808 (Z. Feichi)

<b>Notation</b>	$M$	Gas-to-liquid momentum flux ratio, [-]
<b>Greek Symbols</b>	$MR$	Gas-to-liquid momentum ratio, [-]
$\mu$		Dynamic viscosity, [mPas]
$\nu$		Kinematic viscosity, [m <sup>2</sup> /s]
$\rho$		Density, [kg/m <sup>3</sup> ]
$\sigma$		Surface tension, [N/m]
<b>Latin Symbols</b>	<b>Super-/Subscripts</b>	
$\dot{m}$	$\bar{\cdot}$	Time averaged or filtered values
$\dot{V}$	$\cdot_f$	Values conditioned to $f$
$\mathbf{n}$	$\cdot_G$	Gas phase
$\mathbf{u}$	$\cdot_L$	Liquid phase
$\tilde{k}$	$\cdot_r$	Relative between liquid and gas phase
$A$	$\cdot_S$	Values evaluated for the spray zone
$a, b$	$\cdot_{cell}$	Cell values
$d$	$\cdot_{L,0}$	Values taken from liquid stream within the nozzle
$E_{K_L}$	$\cdot_{rms}$	Time root mean square values
$f$	$\tilde{\cdot}$	Favre-filtered values
$f$	<b>Acronym</b>	
$K$	BTL	Biomass-To-Liquid
$k$	CTL	Coal-To-Liquid
$L_C$	DNS	Direct Numerical Simulation
$p$	EFG	Entrained Flow Gasification
$V$	IGCC	Integrated Gasification Combined Cycle
$x$	LES	Large Eddy Simulation
<b>Dimensionless Numbers</b>	PAT	Pressurized Atomization Test rig
$GLR$	SNG	Synthetic Natural Gas
	VOF	Volume of Fluid Method

## 1. Introduction

Atomization of liquid fuels by coaxial airflow (air-blast or air-assisted) represents one of the most important atomization methods with a widespread application range, for example in aero engines or entrained flow gasification systems [1, 2]. The spray quality as a consequence of the primary atomization close to the nozzle exit has a significant impact on the evaporation and mixing of fuel vapor with oxidizer, which is intimately related to the overall perfor-

mance of the jet engine or the syngas quality in EFG (entrained flow gasification). The breakup process of a liquid jet is governed by the competition between cohesive surface tension force and disruptive aerodynamic forces at the liquid surface. Marmottant and Villermaux [3] showed that the liquid destabilization in case of air-assisted atomization is initialized by a Kelvin-Helmholtz instability, which generates interfacial waves on the liquid core by aerodynamic forces. In a second stage, the surface perturbations grow due to the Rayleigh-Taylor instability, where liquid structures protruding from the liquid surface are accelerated by aerodynamic interactions, leading to disintegration of the intact jet core. This process is usually referred to as primary atomization. If the primary droplets exceed a critical size, they break up further into smaller droplets, a process known as secondary atomization. The primary breakup process covers the formation of unstable waves along with the detachment of first liquid fragments, which determines the production of small droplets during secondary breakup. Therefore, a detailed understanding of the jet breakup stage is a prerequisite for controlling the size, dynamics and the spatial-temporal distribution of the liquid mass near the reaction zone downstream of the atomizer.

Due to limited optical access for detailed measurement of the multiphase flow field, previous experimental works on primary atomization mainly focused on the morphology of the breakup process by shadowgraph images, and developing estimations for some basic properties as a function of the operating parameters, such as the breakup length or the cone angle [4, 5, 6, 7, 8, 9, 10, 11, 12, 13, 14, 15, 16, 17, 18, 19]. Chigier and Faragò [7] classified morphological behaviours of primary atomization into different regimes depending on the gaseous Weber number  $We_G$  and liquid Reynolds number  $Re_L$ . Lasheras et al. [10, 11] suggested the momentum flux ratio  $M$  as an additional important parameter for an universal classification of air-assisted atomization. Different correlations have been proposed for predicting the liquid core length  $L_C$  based on these parameters [6, 9, 10, 13, 16], which showed however only good agreement for their own experimental setups. As different nozzles were applied in these works and the desired measurement values were only hardly distinguishable for many test conditions due to experimental limitations, the available data and correlations are of questionable generality and the physics behind primary atomization is still not well understood. Additionally, it is not sufficient to describe atomization performance solely by scalar geometrical and operational parameters, but the injection direction of the atomizing fluids in relation to each other and to the ambient has to be included [14].

To obtain a more detailed insight into the breakup mechanism, numerical simulations have been conducted in [20, 21, 22, 23, 24, 25, 26, 27, 28, 29]. In these works, dominant phenomena prevailing the gas and liquid interactions are properly resolved, so that morphological behaviours such as rupture of the liquid jet core or the disintegration of liquid ligaments during primary atomization could be reproduced in detail. For instance, Shinjo and Umemura [22] performed direct numerical simulations (DNS) on the primary atomization of a round liquid water jet injected into quiescent high pressure air, showing that ligament formation is triggered by roll-up of the liquid jet tip, and disturbances are fed from the liquid jet tip upstream through vortices and droplet re-collision. In the work by Zandian et al. [23], three atomization cascades were distinguished for the primary atomization of a planar liquid jet based on simulation results from DNS, which were classified in terms of the liquid Reynolds number and gas Weber number. Warncke et al. [29] studied the breakup process of a planar prefilming airblast atomizer with DNS, which showed good agreement with corresponding experiments. Despite the advances made in previous experimental and numerical works, predicting the characteristics of the droplets after primary breakup is challenging, as they are affected by a large number of parameters, such as the design of the nozzle, properties of the fluids and operating conditions. Because these parameters are generally not known in advance, available spray combustion models mostly incorporate drastic simplifications. For example, one common spray model introduces a large number of Lagrangian particles representing liquid droplets with pre-defined properties, which are injected into the computational domain from specified locations downstream of the primary atomization zone and traced during the simulation [30, 31, 32, 33]. Although such models have enabled practical applications, the underlying assumptions often differ from the real primary breakup physics and a number of tuning parameters depending on the flow conditions need to be determined based on limited measurement data or even completely arbitrarily. In addition, most of the experiments and numerical works have been performed for atmospheric conditions with water, although elevated pressures and high-viscous liquid fuels are generally applied in engineering systems. Accordingly, existing knowledge needs to be extended to develop more advanced sub models for predicting spray properties of high-viscous liquids and at elevated pressure conditions.

Objective of this work is therefore to study numerically the effect of elevated pressure on the primary breakup behaviour of a round glycerol/water jet with a dynamic viscosity of 100 mPas (which is 100 times larger than that of pure water) injected into a coaxial airflow and at elevated pressures up to 6 bar. The setup is represented by a generic atomization test rig with a simplified nozzle configuration used by a real-scale entrained flow gasification

(EFG) plant proposed in the framework of the bioliq® process [34, 35], where biogenic residues from the agricultural sector are converted through process-related reactor systems into high-quality, synthesis fuels. The conversion of low grade biogenic energy resources like biomass residues to synthesis gases or syngas through the high-pressure EFG process provides a promising perspective for the efficient reduction of greenhouse gas emissions and energy recovery. The syngas can be used to produce substitute or synthetic natural gas (SNG), basic chemicals, liquid fuels by means of biomass-to-liquid (BTL) or coal-to-liquids (CTL) process, or can directly be used as fuel for operating gas turbines in a combined cycle power plant, e.g. in an integrated gasification combined cycle (IGCC). As carbon in the biomass stems originally from the atmosphere, conversion of such biogenic fuels into other types of energy or chemicals constitutes a carbon neutral process cycle. The production of high-quality, tar-free syngas, however, represents a challenging task: despite the extreme reactor conditions due to the high pressure (up to 80 bar) and high temperature (1200 °C - 1600 °C) environment, viscosity of the liquid fuel may be as large as 1000 mPas. The atomization of liquid fuel, generally through a so-called gas assisted atomizer, has the task to generate a fine spray located at desired locations, which is then evaporated and mixed with oxidizer gas to form a well-defined mixture. From the view point of gasification performance, it is particularly important to avoid large droplets, which may lead to incomplete evaporation due to the short residence time in the gasifier. Accordingly, the atomization of liquid fuel plays a crucial role for the overall conversion rate of the gasification process and is the motivation of the present work.

The simulation conditions for the current work are designed to keep the mass flow rates or the gas-to-liquid mass flow ratio constant while varying the pressure, which represents the basic operating parameter for the EFG process. In addition, the bulk flow velocities of the air and liquid stream are kept constant with varied pressure. In this way, the momentum flux ratio  $M$  and the gaseous Weber number  $We_G$  scale linearly with the pressure  $p$ , so that the effect of reactor pressure can be compared with existing literature in terms of these non-dimensional parameters. One objective is therefore to justify the influence of system pressure on the dynamics of primary atomization in terms of the characteristic dimensionless parameters like  $M$  and  $We_G$ . An additional focus of this work lies on elucidating the behaviour of multiphase momentum exchange at increased pressure.

The work is organized as follows: Sec.2.1 introduces the experimental testrig and measurement conditions, whereas numerical setups including the computational grids and the boundary conditions are described in Sec.2.2. Sec.3.1 and Sec.3.2 compare the simulation and measurement results with regard to the breakup morphology and breakup length. Sec.3.3 is dedicated to validate the grid resolution by means of a twice-refined grid, using otherwise the same operating conditions and numerical setups. Focus of Sec.4 is to assess the kinetic energy in the liquid phase and its correlation with modified pressure. A short summary of the work is given in Sec.5.

## 2. Experimental and Numerical Setups

### 2.1. Experimental conditions

The pressurized atomization test rig (PAT) is used for the experimental study of the primary breakup process at elevated ambient pressure [36]. It consists of a twin-fluid nozzle and an optically accessible pressure chamber. The generic design of the PAT system allows the investigation of specific parameters, such as the reactor pressure, fluid viscosity or nozzle geometry on the atomization process. The cylindrical pressure chamber can be operated at a system pressure up to 21 bar, and has an inner diameter of 300 mm and a height of 3000 mm. The twin-fluid atomizer is mounted on a movable lance with supply of liquid via eccentric screw pumps. A process control system allows for control of gas and liquid mass flows, as well as for regulation of the reactor pressure. A more detailed description of the PAT system can be found in [36]. Figure 1 illustrates the nozzle system used in this work, consisting of a central liquid jet with glycerol/water mixture (glycerol mass fraction equal to 0.843) and a high-speed coaxial airflow. The diameter of the liquid nozzle is  $d = d_L = 2$  mm and the thickness of the nozzle wall for the liquid jet is  $s = 0.1$  mm. The mass flow rate of liquid is  $\dot{m}_L = 20$  kg/h and that of the annular airflow is  $\dot{m}_G = 12$  kg/h, leading to a gas-to-liquid mass flow ratio of

$$GLR = \dot{m}_G / \dot{m}_L = 0.6 \quad (1)$$

The temperatures of liquid and gas streams are 293 K. The pressure  $p$  has been parameterized from 1 to 6 bar. With varied pressure, the geometry of the nozzle is adapted to keep the mass flow rate  $\dot{m}_G$ , the momentum flow  $M_G$  and the velocity  $u_G$  of the gas flow constant. More specifically, the outflow area of the annular gas flow  $A_G$  has been reduced proportionally with increased pressure:  $A_G \propto p^{-1}$  according to  $\dot{m}_G = \rho_G A_G u_G$  and  $\dot{m}_G = const.$ ,  $u_G = const.$  and

$\rho_G \propto p$ . The resulting outer diameters of the gas nozzle  $d_G$  are shown in Fig.1. In this way, the momentum ratio  $MR$ , the liquid Reynolds number  $Re_L$  and the Ohnesorge number  $Oh$  remain constant while changing the pressure:

$$MR = \frac{\rho_G u_G^2 A_G}{\rho_L u_L^2 A_L} = 25, \quad Re_L = \frac{\rho_L u_L d_L}{\mu_L} = 3500, \quad Oh = \frac{\mu_L}{\sqrt{\rho_L d_L \sigma}} = 0.26 \quad (2)$$

with the bulk velocities of the gas and liquid streams  $u_G = const. = 60$  m/s and  $u_L = const. = 1.4$  m/s.  $\rho_L$  and  $\rho_G$  are the liquid and gas density,  $A_L$  and  $A_G$  are the outflow areas of the liquid and gas flows at the nozzle exit. The surface tension of the liquid is  $\sigma = 64.8$  mN/m. Table 1 summarizes additional important dimensionless parameters in dependence of pressure:

$$Re_G = \frac{\rho_G u_G d_{Gap}}{\mu_G}, \quad M = \frac{\rho_G u_G^2}{\rho_L u_L^2}, \quad We_G = \frac{\rho_G u_G^2 d_L}{\sigma} \quad (3)$$

The momentum flux ratio  $M$  and the Weber number  $We_G$  scale linearly with pressure due to the proportional increase of gas phase density with pressure. Both air and glycerol/water mixture have been treated as Newtonian fluids, having the dynamic viscosities of  $\mu_G = 0.018$  mPas,  $\mu_L = 100$  mPas, and densities of  $\rho_{G,1bar} = 1.205$  kg/m<sup>3</sup>,  $\rho_L = 1223$  kg/m<sup>3</sup>.

**Table 1**

Characteristic dimensionless parameters.

$p$ [bar]	$Re_G$ [-]	$M$ [-]	$We_G$ [-]
1	11,400	1.7	128
2	14,400	3.4	256
6	19,000	10.2	768

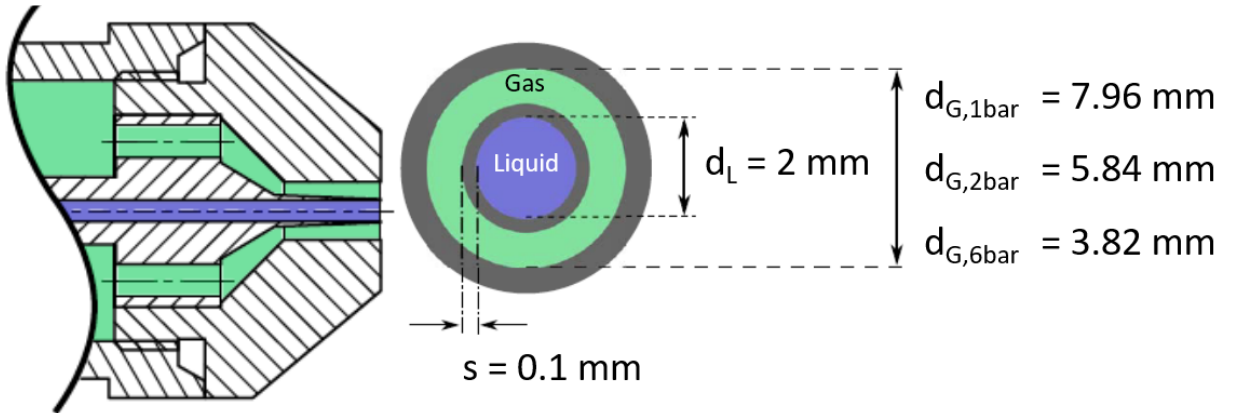


**Figure 1:** Geometrical dimensions of the twin-fluid atomizer.

## 2.2. Numerical Setups

The computational domain covers a major part of the nozzle geometry in order to resolve the internal flow within the nozzle. The liquid inlet starts from an extension of  $5d$  and the annular air at a distance of  $12.5d$  upstream the nozzle exit plane. The nozzle part is connected to a cone-shaped domain downstream, as depicted in Fig.2 on the left, which has a length of  $30d$  and diameters of  $10d$  and  $20d$  at the nozzle exit and at the outlet. The domain length has been selected based on a compromise in terms of simulation accuracy and available computational resources. It allows use of refined grid resolution and the outlet plane lies sufficiently far away from the jet core, so that “zero gradient” type boundary condition can be reasonably applied. The  $x$ -axis indicates the streamwise direction and the origin of

the coordinate system is located at the centre of the nozzle outlet. The computational grids used for different pressure conditions consist of approx. 11 million hexahedral elements, which are locally refined close to the liquid jet with a smallest resolution of  $\Delta_{min,r} = 25 \mu\text{m}$  and  $\Delta_{min,x} = 50 \mu\text{m}$  in radial and streamwise directions. As the resolution is not sufficient to resolve the whole range of length scales of droplets for the given conditions with high  $We_G$  and  $Re_G$ , particular focus of this work is laid on studying the primary breakup behaviour of intact liquid core in dependence of pressure.

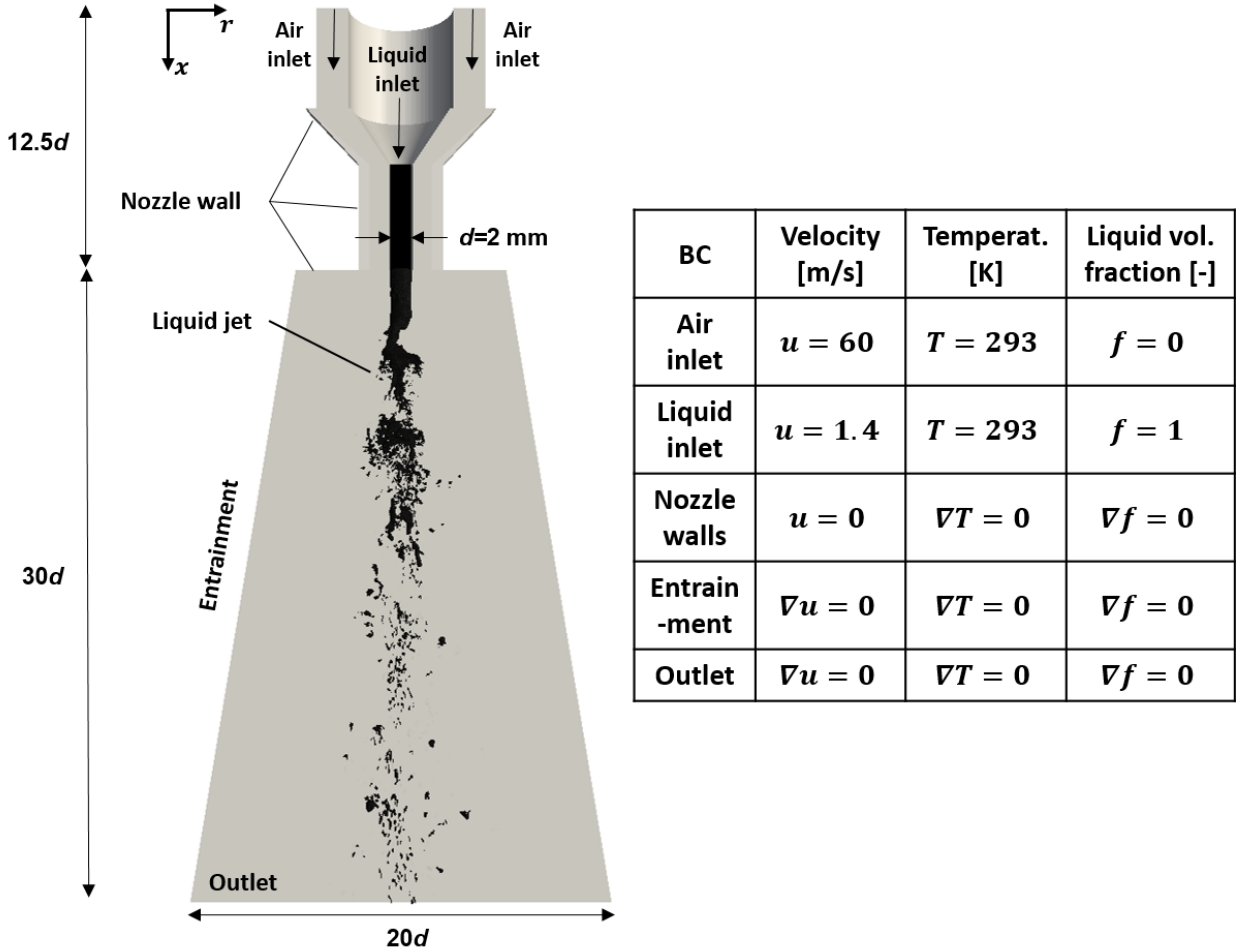


Figure 2: Computational domain (left) and list of boundary conditions (right).

OpenFOAM-v1806 [37] has been used to simulate the multiphase flow, employing the volume of fluid (VOF) method for capturing the gas-liquid interface [38, 39]. The VOF method represents one of the most common approaches for modeling multiphase flows and has already been extensively validated in previous works [21, 22, 20, 24, 26, 27, 29, 40]. The liquid and gas phases in VOF are treated as a virtual fluid and a balance equation is solved for the volume fraction of liquid  $f$

$$\partial_t f + \nabla \cdot (\tilde{\mathbf{u}} f) = \nabla \cdot (f(1-f)\tilde{\mathbf{u}}_r) \quad (4)$$

in addition to the general governing equations for the total mass, the momentum and the energy

$$\partial_t \bar{\rho} + \nabla \cdot (\bar{\rho} \tilde{\mathbf{u}}) = 0 \quad (5)$$

$$\partial_t (\bar{\rho} \tilde{\mathbf{u}}) + \nabla \cdot (\bar{\rho} \tilde{\mathbf{u}} \tilde{\mathbf{u}}) = -\nabla \bar{p} + \nabla \cdot (\bar{\tau} + \bar{\tau}^{sgs}) + \bar{\rho} \mathbf{g} + \bar{\mathbf{F}}_\sigma \quad (6)$$

$$\partial_t (\bar{\rho} \tilde{\epsilon}) + \nabla \cdot (\bar{\rho} \tilde{\epsilon} \tilde{\mathbf{u}}) = -\nabla \cdot (\bar{\rho} \tilde{\mathbf{u}}) - \nabla \cdot (\bar{\mathbf{j}}_q + \bar{\mathbf{j}}_q^{sgs}) \quad (7)$$

In Eq.(4-7),  $\bar{\cdot}$  denotes spatially filtered and  $\tilde{\cdot}$  Favre-filtered values in the framework of large eddy simulation (LES) of a compressible flow.  $\rho$  is the gas density,  $\mathbf{u}$  the velocity vector,  $p$  the pressure and  $\mathbf{g}$  the gravitational acceleration.  $\bar{\mathbf{F}}_\sigma = \sigma \kappa \nabla f$  denotes the volumetric surfaces tension forces and  $e = \int_0^T c_v dT + 0.5|\mathbf{u}|^2$  the specific total energy, where  $\kappa$  is the curvature of the interface,  $c_v$  the isochoric heat capacity and  $T$  the temperature. The shear stress tensor caused by gradients of flow velocities is given by  $\tau = \mu(\nabla \mathbf{u} + \nabla \mathbf{u}^T - \frac{2}{3} \nabla \cdot \mathbf{u} I)$  with the unit tensor  $I$ .  $\bar{\mathbf{j}}_q = -\lambda \nabla T$  is the heat flux due to thermal conduction, with  $\lambda$  being the thermal conductivity. The relative velocity  $\mathbf{u}_r$  between the liquid and gas phases in Eq.(4), also called compression velocity, is calculated from

$$\mathbf{u}_r = \mathbf{u}_L - \mathbf{u}_G = |\mathbf{u}| \mathbf{n} = |\mathbf{u}| \frac{\nabla f}{|\nabla f|} \quad (8)$$

where  $\mathbf{n}$  is the surface normal unit vector [43]. In this way,  $f = 1$  indicates the pure liquid phase and  $f = 0$  the pure gas phase. Consequently, the intermediate values with  $0 < f < 1$  identify the gas-liquid interface. The material properties of the liquid-gas mixture, i.e., the density and the viscosity, are calculated based on the volume-weighted average in terms of  $f$ .

$$\rho = f \cdot \rho_l + (1 - f) \cdot \rho_g, \quad \mu = f \cdot \mu_l + (1 - f) \cdot \mu_g \quad (9)$$

The subgrid scale (SGS) stress tensor  $\bar{\tau}^{sgs} = \bar{\rho}(\bar{\mathbf{u}}\bar{\mathbf{u}} - \bar{\mathbf{u}}\bar{\mathbf{u}})$  and SGS heat flux  $\bar{\mathbf{j}}_q^{sgs} = \bar{\rho}(\bar{\mathbf{u}}\bar{e} - \bar{\mathbf{u}}\bar{e})$  in Eq.(6) and Eq.(7) are evaluated from the SGS turbulence modeling [41]. The wall-adapted local eddy viscosity (WALE) model has been applied in the current work to account for these unresolved SGS fluxes.

The boundary conditions used for  $\mathbf{u}$ ,  $T$  and  $f$  are listed in Fig.2 on the right. There, no-slip condition was used for the velocity on the nozzle walls, whereas the velocities of the gas and liquid inlets were computed according to the given mass flows. At the entrainment and outlet boundaries, gradients of  $\mathbf{u}$ ,  $T$  and  $f$  were set to zero.  $T$  was prescribed at 293 K at the inlets,  $f$  was equal to zero at the gas inlet and unity at the liquid inlet. The total pressure was set to the system pressure at the entrainment and outlet planes, and the pressure gradients at the inlets were adjusted to provide the specified mass fluxes.

The balance equations have been solved in a fully compressible formulation, employing an implicit scheme of 2nd order accuracy (CrankNicolson) for time integration and 2nd order schemes for discretization of the convection terms. The time step is set to  $\Delta t = 0.2 \mu s$ , keeping the maximum CFL number below 0.5. Statistical averaging of the flow has been performed for a physical time of 80 ms or 400,000 time steps, which corresponds to more than 10 flow-through times based on the bulk velocity of liquid stream and the breakup length (see Fig.4).

### 3. Simulation Results

#### 3.1. Breakup Morphology

The following sections present the simulation results based on the locally resolved liquid volume fraction  $f$ , with  $\bar{f}$  and  $f_{rms}$  denoting its time averaged and root mean square (rms) values. Figure 3 on the left compares the simulated instantaneous liquid jet visualized by line-of-sight integrated liquid volume fraction  $f$  with snapshot of the liquid jet recorded with a high-speed camera for  $p = 6$  bar. Both simulation and measurement identify a pulsating-mode instability of the liquid jet core accompanied by disintegrations of fibre-type liquid fragments. The morphological behaviours are in accordance with the breakup regimes classified by Chigier and Faragò [7] based on  $Re_L$  and  $We_G$ , i.e., fibre-type for  $100 < We_G < 500$  and with a dominance of the super-pulsating mode for further increased  $We_G$ . As the current grid resolution is not able to reproduce the secondary breakup process in detail, a direct comparison of calculated and measured liquid fragments in downstream region is not feasible. The effect of grid resolution on the primary and secondary atomization is further discussed in section 3.3 (see e.g. Fig.6).

The breakup mechanism of the liquid jet due to aerodynamic force is elucidated in Fig.3 on the right by the instantaneous contours of the streamwise velocity on a meridian cut-plane. In this case, initial turbulence is generated already within the nozzle in the boundary layers that develop along the nozzle wall (in terms of turbulent channel flow). Outside the nozzle, the shear layer between the high-speed airflow and the low-speed liquid jet results in formation of coherent vortices or flow instabilities near the nozzle, which break down further to a fully turbulent flow. The breakup process of the liquid core is prevailed by the turbulent flow through multiphase interaction or momentum exchange between different phases. In Fig.3, the intact jet core is identified by the iso-surface of  $f = 0.5$ . In a first step, the intact liquid jet is disturbed by the high-speed airflow, which causes local recirculation zones of the gas flow along the



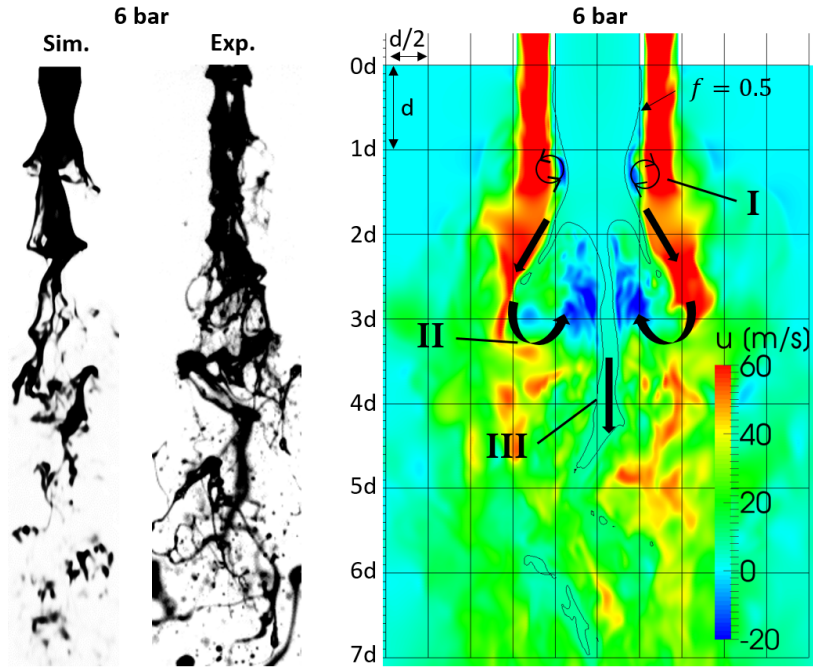


**Figure 3:** Left: comparison of calculated liquid jet visualized by line-of-sight integrated liquid volume fraction with snapshot from high speed imaging. Right: instantaneous contours of streamwise velocities illustrating the breakup mechanism of liquid core through aerodynamic interference.

liquid surface and a decrease of the diameter of the liquid column (stage I in Fig.3, blue colour indicates negative flow velocity, i.e., back flow). Further downstream, a large concentric, axisymmetric ring vortex is generated around the jet due to shear forces exerted on the gas flow at the interface. These vortices penetrate into the liquid jet from its tip and cause strong recirculation zones there, which hinder the growth of the intact jet core towards the downstream direction (indicated in Fig.3 as stage II). At the same time, the protruding tip of the liquid jet is elongated by the airflow at the outer edge and the centre, leading to a M-shaped structure. Finally, these tips of the jet core are thinned by aerodynamic stretching and first liquid ligaments pinch off from the jet (stage III). Although not shown here, the same behaviour regarding the breakup morphology and mechanism with pulsating mode instability and fibre-type disintegration has been confirmed to be qualitatively similar for other pressure conditions. The streamwise distance, at which the jet breakup occurs, has however been confirmed to be decreased with increasing pressure.

### 3.2. Breakup Length

The breakup length  $L_C$  is defined by the length of the continuous, coherent portion of the liquid jet attached to the nozzle. In this case, the breakup process results in an abrupt jump of  $f$  from 1 (intact liquid core) to 0 (air) along the jet axis, leading to spatial discontinuities and temporal fluctuations of  $f$ . According to  $0 \leq f \leq 1$ , the maximal possible value of  $f_{rms}$  is 0.5, which occurs only under the conditions of  $\bar{f} = 0.5$  and a bimodal distribution or fluctuation of  $f$  with equally weighted probabilities for  $f = 0$  and  $f = 1$ . Therefore, it is reasonable to identify  $L_C$  with the locations of the maximum of  $f_{rms}$  or  $\bar{f} = 0.5$ , respectively. Figure 4 shows profiles of  $\bar{f}$  and  $f_{rms}$  along the centreline axis  $x$ .  $\bar{f}$  decreases faster from 1 to 0 with increased pressure, denoting a reduction of the liquid core length with pressure. The same behaviour can also be perceived from the profiles of  $f_{rms}$ , where its maximum value with  $f_{rms,max} \approx 0.5$  (indicated in Fig.4 by the horizontal line) shifts towards smaller  $x/d$  with increased pressure. As expected, the  $x/d$  positions with  $f_{rms,max} \approx 0.5$  correspond closely with the locations of  $\bar{f} \approx 0.5$  (see the intersection points between  $\bar{f}$  and  $f_{rms}$  in Fig.4), confirming the equally distributed bimodal behaviour of  $f$  during breakup of the liquid jet.

As liquid fibres stripped-off the periphery of the jet core obscure observation of the central liquid jet, a direct assessment of jet disintegration along the centreline is difficult from the view of line-of-sight measurement. Therefore,  $L_C$  evaluated from experiment is based on finding the first breakup locations of the primary ligaments along the

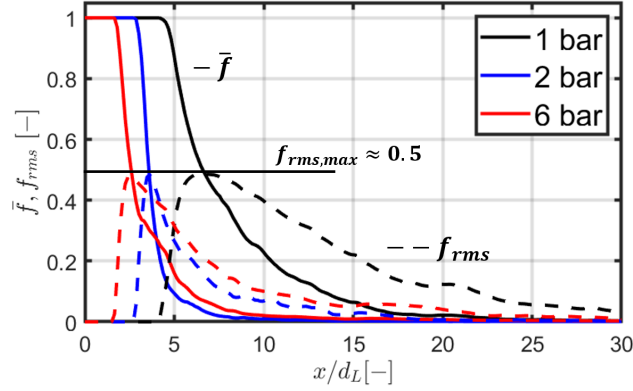


**Figure 4:** Streamwise profiles of time-mean and rms values of liquid volume fraction at different pressures.

streamwise axis using image processing techniques. Consequently, the measured  $L_C$  are considerably larger than the calculated  $L_C$  determined with  $f_{rms,max}$ , as shown in Fig.5 on the left for measured and on the right for calculated data from the simulations. The standard deviations of measured  $L_C$  have been indicated in Fig.5 on the top left side with error bars and on the bottom left side with dashed lines. The evolution of  $L_C$  vs.  $p$  has been fitted by a power function and shown in Fig.5. The calculated exponent of the power law has been evaluated to  $b = -0.51$ , which is in quantitatively good agreement with experimentally determined values around -0.5 with respect to  $We_G$ ,  $M$ , or  $\rho_G/\rho_L$ , although different nozzle configurations with water jets and atmospheric condition were applied in these works [4]. Accordingly, the effect of elevated pressure on  $L_C$  can be reproduced equivalently in terms of  $M$  and  $We_G$ , which scale linearly with pressure. In addition, the calculated exponent of the power law with  $b = -0.51$  agrees well with the fitting coefficient  $b = -0.49$  obtained in previous simulations of a similar nozzle at elevated pressures and applying the same liquid [42]. Note that only 3 points, corresponding to the three available measured pressure conditions, are used here, which represents a source of uncertainty with respect to the fitting coefficients. The power-law fitting proposed in this work has been made in an analogous manner to previously obtained power-law correlations from experiments [4], which should be regarded as a first-order estimate for the considered twin-fluid nozzle setup.

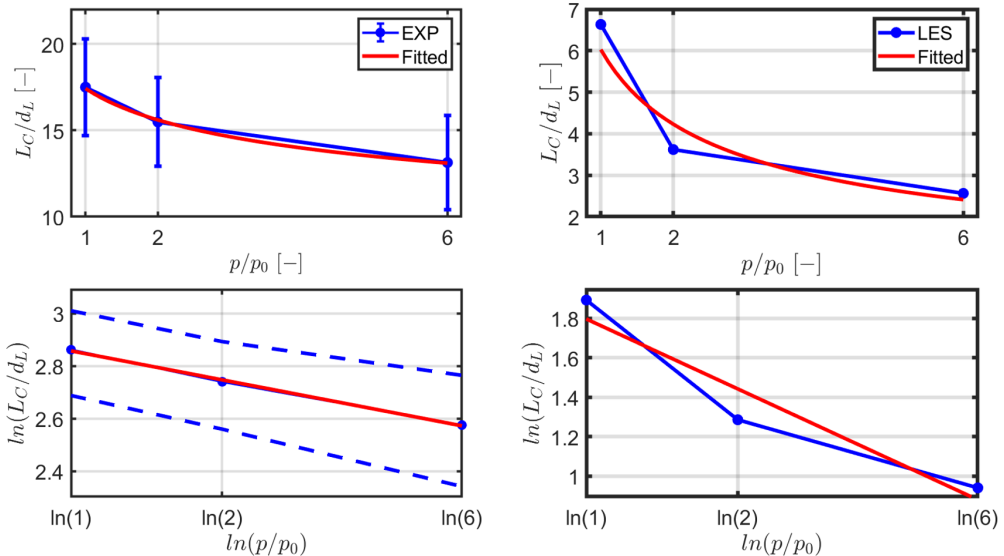


**Figure 5:** Comparison of measured (left) and calculated (right) breakup lengths  $L_C$  in dependence of pressure, along with their fitted data from a power law function: at the top with linear scaling and at the bottom with log-log scaling.

### 3.3. Effect of Grid Resolution

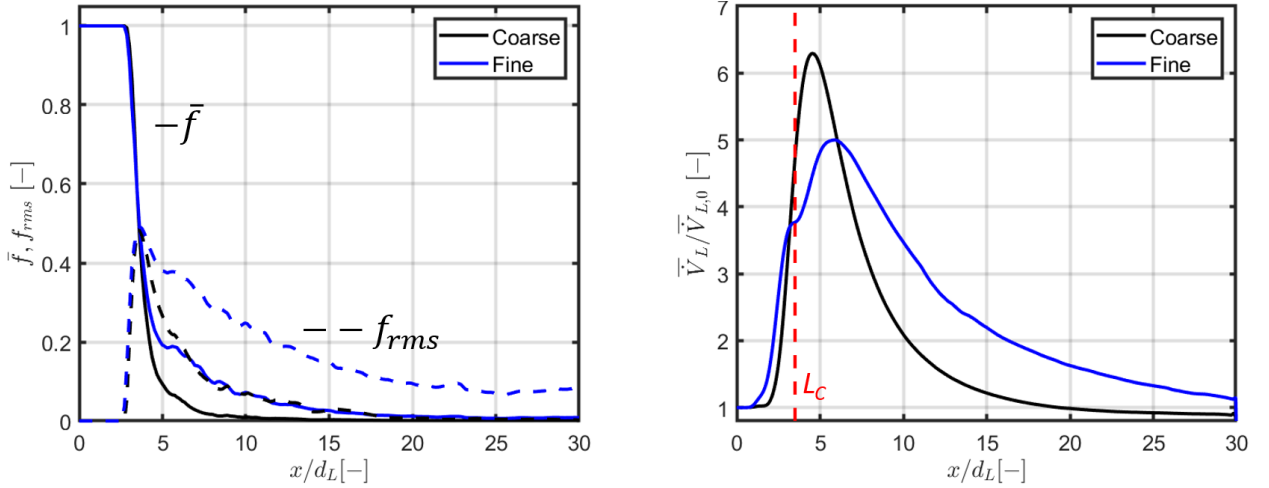
In order to justify the results obtained in the last section, simulations with twice-refined grid resolutions have been carried out for the case with  $p = 2$  bar, applying a minimum cell size of  $\Delta_{r,min} = 12.5 \mu\text{m}$  and approx. 84 million cells. Note that both VOF and LES techniques are essentially grid-dependent procedures by definition, because they resolve the gas-liquid interface, the droplets and the turbulent flow down to a cut-off scale given by the cell size. An increased grid resolution allows reproducing smaller liquid elements and reduces the influence of numerical as well as turbulent diffusion, leading to an enhanced multiphase interaction. The computational cost increases however by a factor of 16 by using a twice-refined grid resolution (for 8 times more grid cells and twice-reduced simulation time step).

Figure 6 compares instantaneous liquid cores identified with iso-surfaces of  $f = 0.5$  from simulations using the coarse and the fine grids. The breakup morphology obtained with both grids are essentially similar, yielding a pulsating mode instability and fibre-type liquid fragments. However, it is evident that substantially more primary ligaments and small-scale liquid fragments downstream of the liquid jet are reproduced by the fine grid simulations, which yields a better comparison of the simulation with high-speed imaging (see the left part of Fig.6). The result confirms the significant impact of grid resolution on resolving small-scale liquid structures in the framework of VOF-LES, in particular for the downstream regions of the liquid jet core. Consequently, the fine grid leads to an increase of overall resolved liquid volume within the computational domain compared to the coarse grid. In Fig.6, small-scale disturbances on the liquid jet surface are underestimated in the simulations. One reason may be attributed to the under-resolved turbulent flow fluctuations in the nozzle, e.g. the boundary layer along the nozzle wall cannot be fully resolved by using the current grid resolution.



**Figure 6:** Comparison of side views of instantaneous liquid jets identified with  $f = 0.5$  iso-surfaces from VOF-LES using different grid resolutions with one measured snapshot (left) for  $p = 2$  bar.

Figure 7 on the left plots streamwise distributions of  $\bar{f}$  and  $f_{rms}$  calculated by using different grid resolutions, where  $L_C$  identified by  $f_{rms,max}$  (see Fig.4 too) remain nearly the same for simulations using the coarse and fine grids. In addition, the streamwise profiles of  $\bar{f}$  and  $f_{rms}$  calculated from both grids are almost identical up to the location of  $L_C$  and they deviate from each only after the breakup distance with  $x > L_C$ .  $\bar{f}$  and  $f_{rms}$  from the fine mesh decrease slower or are larger compared with the coarse mesh, which is attributed to the better resolved secondary breakup process downstream of the intact core by using the fine grid (see Fig.6).



**Figure 7:** Comparison of calculated streamwise profiles of  $\bar{f}$ ,  $f_{rms}$  (left) and normalized liquid volume flux  $\bar{V}_L$  (right) using a coarse and a fine grid for  $p = 2$  bar.

The same behaviour can also be detected in Fig.7 on the right, showing the time averaged liquid fluxes  $\bar{V}_L = \int \bar{f} \bar{u}_L dA$  [ $m^3/s$ ] obtained from surface integrals on axial planes for different grid resolutions. The breakup length is marked with the dashed vertical line. The fine mesh yields a larger  $\bar{V}_L$  in the range of  $x < L_C$ , indicating that the intact jet core is accelerated stronger in this case.  $\bar{V}_L$  increases further for  $x > L_C$  until a maximum value is reached, which reflects the scenarios of stretching the primary ligaments by surrounding gas flow. The gas flow velocity decreases further downstream due to diffusive transport and the primary ligaments break down into small fragments due to secondary breakup, resulting in a decrease of  $\bar{V}_L$  at large  $x$  down to approx.  $\bar{V}_{L,0}$  (liquid volume flux within the nozzle). However,  $\bar{V}_L$  is considerably larger for the fine mesh in the downstream region with  $x/d_L > 10$ , revealing a larger volume of resolved liquid fragments in the secondary breakup or the spray zone. The differences in calculated spray characteristics downstream the primary breakup zone from the coarse and fine grids are essentially shaped by the limitations of the VOF and LES methods by resolving the multiphase flow till the cut-off scale, where numerical diffusion leads to elimination of liquid phase volume with small  $f$  due to the lack of grid resolution. Nonetheless, dominant behaviours regarding primary atomization, such as the breakup morphology and breakup length, as well as the influence of pressure on these, have been confirmed to be grid-independent, justifying the applicability of the ‘‘coarse’’ grid (25  $\mu m$ ) for studying the current primary breakup of co-axial liquid jet by surrounding airflows.

## 4. Multiphase Momentum Exchange

### 4.1. Kinetic Energy of Liquid

The breakup of the liquid jet is caused by the momentum exchange or aerodynamic force exerted by the high-speed gas flow on the low-speed liquid jet, which leads to an increase of the kinetic energy in the liquid phase and acceleration of liquid volumes according to conservation of momentum. In general, large liquid phase velocities  $u_L$  or kinetic energies  $\frac{1}{2}\rho_L u_L^2$  are attributed to small liquid fragments with small  $f$  or low liquid content. For instance, small droplets have commonly larger velocities compared with the liquid core or large liquid ligaments. Therefore, solely  $u_L$  or  $\frac{1}{2}u_L^2$  is not sufficient or representative for assessing quantitatively the absolute kinetic energy in the liquid phase. Accordingly, the kinetic energy from the liquid phase is determined by the product of  $f$  [ $m^3/m^3$ ] and  $\frac{1}{2}\rho_L u_L^2$  [ $J/m^3$ ], revealing the integral kinetic energy of the liquid phase averaged locally over the cell volume [ $J/m^3$ ]

$$k_L = \frac{1}{2} f \rho_L \mathbf{u}_L^2 \quad (10)$$

In the VOF formulation, the resolved flow velocity is given by a weighted mean of the liquid phase  $\mathbf{u}_L$  and gaseous

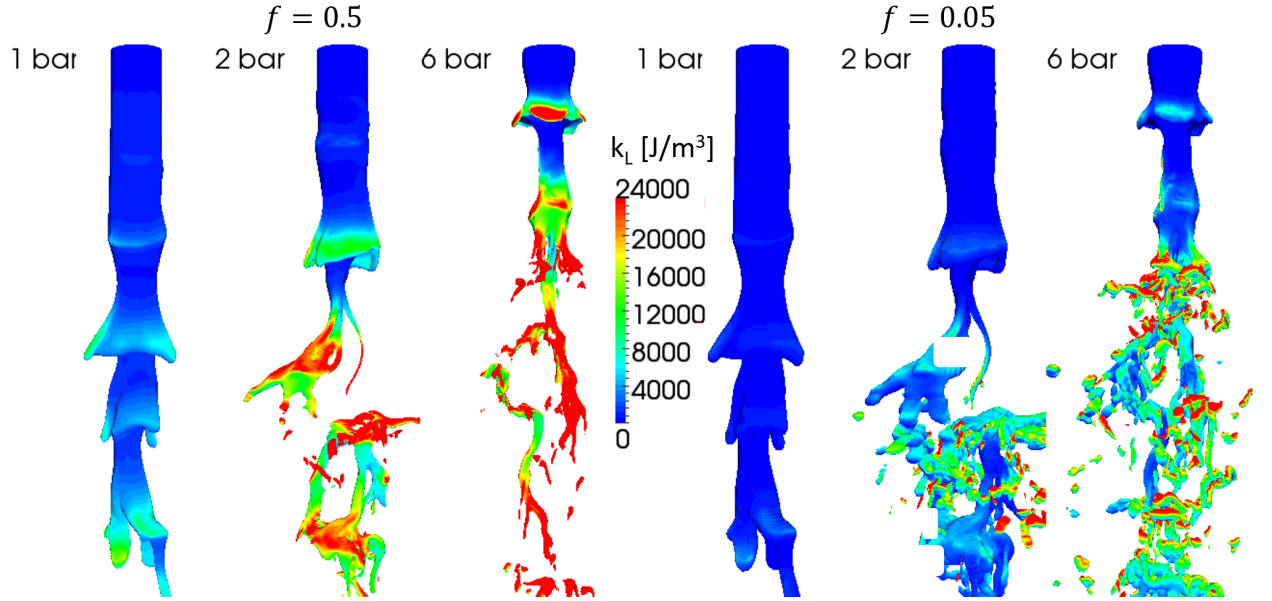
phase velocity  $\mathbf{u}_G$  with regard to  $f$

$$\mathbf{u} = f \mathbf{u}_L + (1 - f) \mathbf{u}_G \quad (11)$$

By combining Eq.(11) and Eq.(8),  $\mathbf{u}_L$  required for the computation of  $k_L$  in Eq.(10) can then be evaluated

$$\mathbf{u}_L = \tilde{\mathbf{u}} + (1 - f) \mathbf{u}_r \quad (12)$$

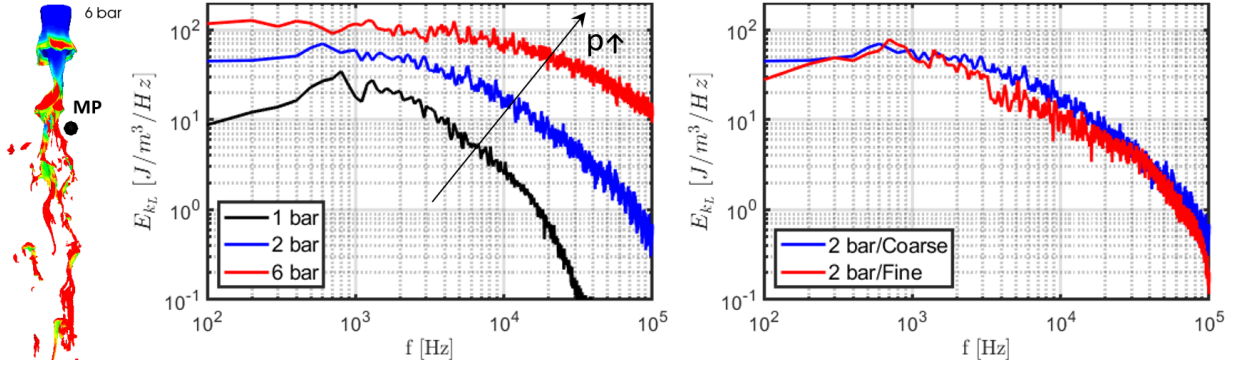
Figure 8 shows instantaneous contours of  $k_L$  for two  $f$  iso-surfaces: on the left for  $f = 0.5$  representing the intact jet core and on the right for  $f = 0.05$  illustrating primary disintegrated liquid fragments. The wavy liquid surface structure caused by the aerodynamic interaction and the decrease of the breakup length with pressure can be detected again (see Fig.3-Fig.5).  $k_L$  increases with pressure and is strongly correlated with the curvature of the gas-liquid interface. As shown in Fig.8 on the left,  $k_L$  is larger at locations with protruding liquid surface, covering the range of negative curvatures (convex towards gas phase), and vice versa for concave jet surface with positive curvatures. In addition, more small-scale liquid fragments with higher  $k_L$  are formed in case of elevated pressure (see Fig.8 on the right), indicating an enhanced breakup of the liquid jet. As the mass flow rate and momentum of the liquid stream are kept constant while varying the pressures, an increase in  $k_L$  denotes specifically a reinforced transfer of momentum from the gas to the liquid phase. Although  $k_L$  is linearly related to  $f$ ,  $k_L$  from both  $f = 0.5$  and  $f = 0.05$  iso-surfaces are of similar order of magnitude for the high pressure case with  $p = 6$  bar. The result reveals a stronger acceleration of disintegrated liquid elements represented by small  $f$  through aerodynamic forces, compared with the intact jet core denoted by large  $f$ .



**Figure 8:** Instantaneous contours of specific liquid kinetic energy at different pressures: on the left for the iso-surface of  $f = 0.5$  and on the right for the iso-surface of  $f = 0.05$ .

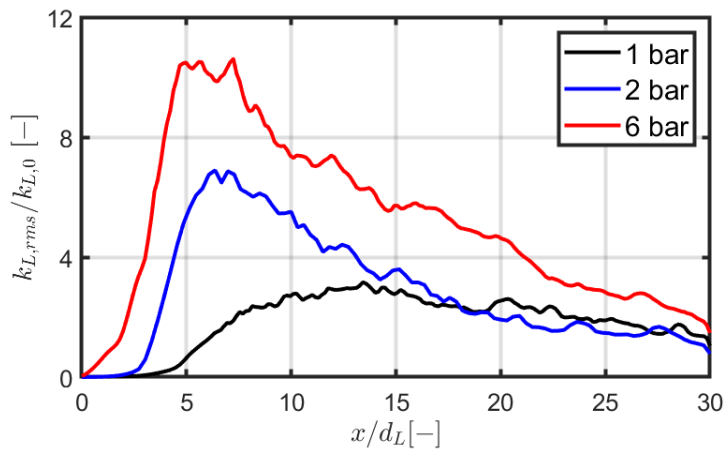
Figure 9 shows the spectral density of liquid kinetic energy  $E_{k_L}$  for one monitor point close to the nozzle, as indicated in Fig.9 on the left by contours of  $k_L$  on the liquid surface with  $f = 0.5$ .  $E_{k_L}$  is calculated from Fourier transformation of temporally sampled  $k_L$  signals, which represents a measure of the turbulent kinetic energy available in the liquid phase. As shown in Fig.9 on the left,  $E_{k_L}$  is larger at elevated pressure in the whole frequency range, which is attributable to the reinforced breakup of liquid jet at elevated pressure. In this case, the jet core breaks down faster into fragments under high-pressure conditions for the considered probe location, whereas breakup of the liquid jet takes place further downstream for the low pressure cases (see Fig.8). The increase of  $E_{k_L}$  with pressure confirms again the higher multiphase momentum transfer at elevated pressure. The differences in  $E_{k_L}$  evaluated for different pressures are particularly large in the high frequency range, pointing out a more intensive small-scale multiphase interaction at elevated pressure. The reason is due to the increased gas phase Reynolds number with pressure (see

Tab.1), which leads to enhanced turbulent fluctuations in the high frequency or high wave-number range dominated by small-scale turbulent vortices. In Fig.9 on the right, simulations using different grid resolutions (as described in Sec.3.3) reveal almost identical spectral distributions of  $k_L$ . The reason is attributable to the well-resolved turbulent flow and the primary breakup of the jet near the nozzle exit on both coarse and fine grids. As a consequence, the same breakup length can be deduced for both coarse and fine grid, as shown in Fig.7 on the left, which confirms again the grid-independence behaviour with respect to the breakup characteristics by using the current grid resolution.



**Figure 9:** Spectral density of specific kinetic energy of liquid  $E_{k_L}$  for a monitor point (MP) close to the nozzle exit:  $x = 4d$ ,  $r = \frac{d}{2}$ , which is illustrated on the left along with the iso-surface of  $f = 0.5$  for  $p = 6$  bar. The left part compares  $E_{k_L}$  for different pressure conditions and the right part compares  $E_{k_L}$  obtained for  $p = 2$  bar by using different grid resolutions.

The same behaviour can be detected in Fig.10 by the streamwise profiles of the time-rms values of  $k_L$  for different pressures, which is normalized to the specific kinetic energy of liquid within the nozzle ( $k_{L,0} = \frac{1}{2}\rho_L v_L^2$ ).  $k_{L,rms}$  represents a measure of the turbulent kinetic energy available in the liquid phase. In comparison with the axial profiles of  $\bar{f}$  shown in Fig.4,  $k_{L,rms}$  increases with decreasing  $\bar{f}$ , revealing an increased kinetic energy or momentum transfer during primary atomization.  $k_{L,rms}$  decreases further downstream due to the entrainment of ambient air, which slows down the gas and liquid flows.  $k_{L,rms}$  is larger and starts to increase at a smaller  $x$  distance at elevated pressure, which correspond to the previously noticed decrease of breakup length and reinforced multiphase momentum transfer with increased pressure.



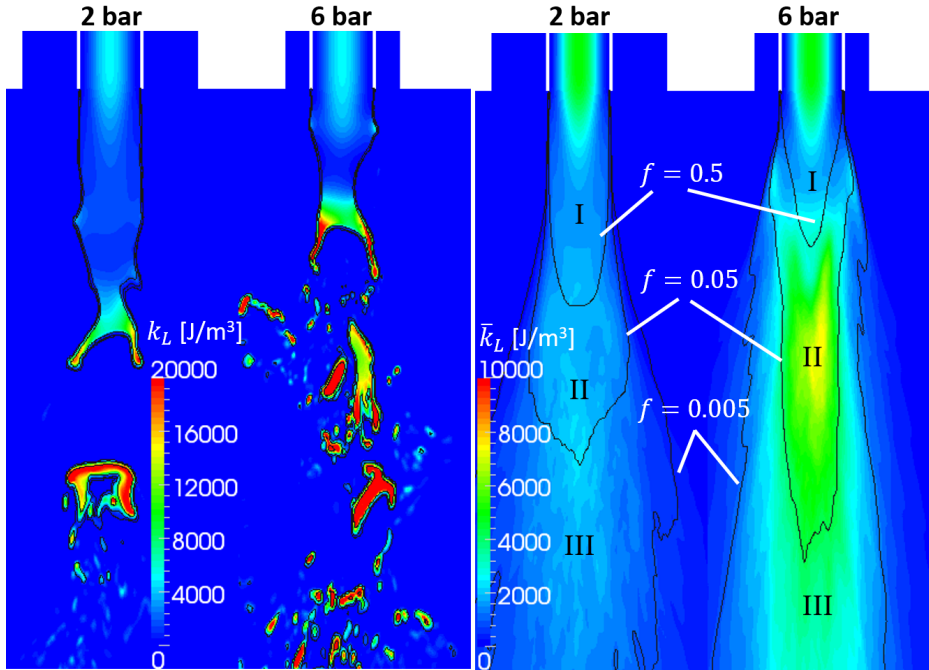
**Figure 10:** Comparison of streamwise profiles of rms values of specific kinetic energy of liquid at different pressures.

Figure 11 illustrates instantaneous (left) and time-mean (right) contours of  $\bar{k}_L$  for  $p = 2$  and 6 bar on a meridian cutting-plane passing through the streamwise axis, together with iso-contours of  $f$ ,  $\bar{f} = 0.5, 0.05$  and 0.005.  $k_L$  is larger at the tips of the jet with protruding liquid ligaments, confirming again the strong correlation of  $k_L$  with curvature of the liquid surface (see Fig.6) and the mechanism of momentum transfer through the ring vortices shown in Fig.3

on the right. In addition, comparison of  $k_L$  from 2 and 6 bar yields an increase of  $k_L$  with pressure, indicating an enhanced momentum exchange at elevated pressure. The differences between the instantaneous  $f$  iso-contours shown on the left of Fig.11 are not apparent, as a sharp gas-liquid interface with  $0 < f < 1$  is resolved by the simulation. The time-averaged contours of  $f$  and  $k_L$  shown on the right of Fig.11 allow however to identify three distinct stages of the atomization process:

- Stage I with the intact liquid core, enclosed by  $\bar{f} = 0.5$ .  $\bar{k}_L$  is relatively small due to low velocity of the liquid stream and the recirculating flows caused by the ring vortices, which hinder growth of the liquid jet (see Fig.3 on the right).
- Stage II with primary disintegrations of liquid fragments, enclosed by the isolines of  $\bar{f} = 0.5$  and 0.05. Liquid fragments pinched off from the intact jet core are accelerated strongly by the coflow air, which leads to a significant increase of  $\bar{k}_L$ .
- Stage III given by dispersed liquid fragments flying into the ambient, within the range of  $0.005 < f < 0.05$ .  $\bar{k}_L$  decreases due to slowdown of gas phase velocity through the entrainment of ambient air.

Note that the borders with  $\bar{f} = 0.5, 0.05$  and  $0.005$  are representatively selected here to distinguish different atomization zones, which are vitally dependent on each other. In this context, the primary breakup process may be covered by a transition from zones I to II and the secondary breakup by the zones II and III (see Fig.11 on the right).



**Figure 11:** Instantaneous (left) and time-mean (right) distributions of specific liquid kinetic energy on a cutting-plane passing through the centerline axis for  $p = 2$  and 6 bar, along with iso-contours of  $f = 0.005, 0.05$  and  $0.5$ .

## 4.2. Spray Dynamics

After primary breakup of the core jet, large liquid fragments are dispersed and further broken into smaller pieces by interacting with the turbulent gas flow, forming a spray downstream the liquid jet core. As the droplet size distribution cannot be resolved or it is essentially dependent on the grid resolution (as shown in Fig.6), the kinetic energy carried by certain droplet size cannot be reproduced by the current LES-VOF approach. Instead, a first-order estimation of liquid phase energy attributed to specified  $f$  range is attempted in this work, assuming a positive correlation between  $f$  and the droplet size. In this way, the liquid kinetic energy per unit liquid volume [J/m³] in the spray zone has been

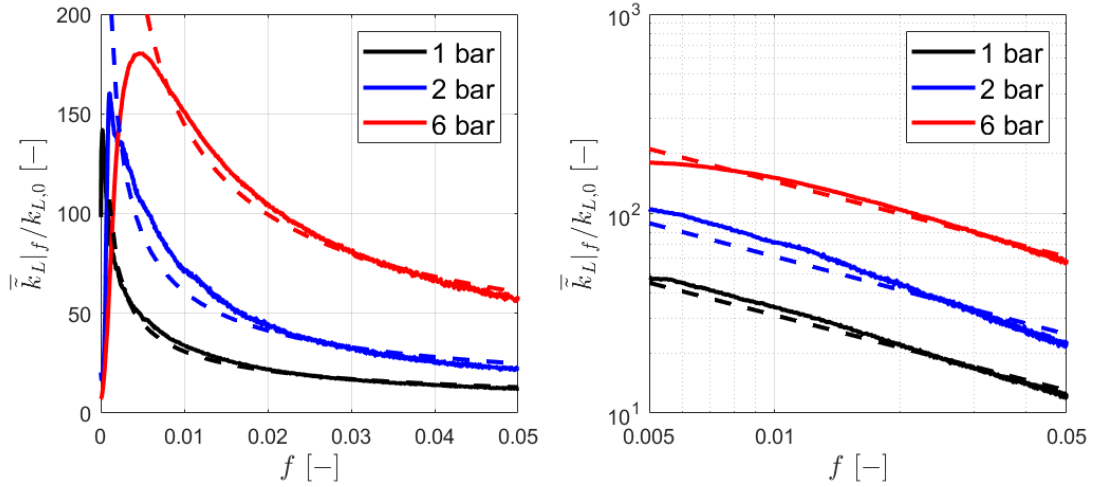


**Figure 12:** Comparison of calculated time averaged kinetic energy density  $\tilde{k}_{L|f}$  conditioned to  $\bar{f}$  at different pressures: solid lines indicate calculated values from VOF-LES and dashed lines fitted curves using an exponential function. Left part is plotted with linear scale and right part on a double logarithmic scale.

evaluated from the simulations by

$$\tilde{k}_{L|f} = \frac{K_{L|f}}{V_{L|f}} \quad (13)$$

with the total volume  $V_{L|f}$  and kinetic energy  $K_{L|f}$  of liquid conditioned to  $f$ . These are calculated from numerical integrations to sum up liquid volumes and kinetic energies for a number of pre-defined equidistant bins of  $f$

$$V_{L|f} = \int f dV|_{\Delta f} = \sum f V_{cell}|_{\Delta f}, \quad K_{L|f} = \int k_L dV|_{\Delta f} = \sum k_L V_{cell}|_{\Delta f} \quad (14)$$

By doing so,  $\tilde{k}_{L|f}$  measures the kinetic energy density (per unit liquid volume) or the velocity of liquid droplets by  $v_p|_f = \sqrt{2\tilde{k}_{L|f}/\rho_L}$  conditioned to specified  $f$  in the spray.

Figure 12 plots time-averaged  $\tilde{k}_{L|f}$  against  $\bar{f}$  calculated for the spray zone represented by the range of  $0.005 < \bar{f} < 0.05$  (stage III indicated in Fig.11 on the right) and using a  $\bar{f}$ -bin size of  $5 \cdot 10^{-5}$ . For all pressure conditions,  $\tilde{k}_{L|f}$  increases with decreasing  $\bar{f}$  till a maximum and it decreases further to 0 at  $\bar{f} = 0$ , when there is no liquid. The increase of  $\tilde{k}_{L|f}$  with reduced  $\bar{f}$  is in accordance with the fact that small droplets associated with small liquid volume fractions have a high kinetic energy due to their small inertia. The turnover point with maximum values of  $\tilde{k}_{L|f}$  shifts to larger  $\bar{f}$  with increased pressure, which is attributable to the more intensive turbulent momentum exchange due to a higher  $Re_G$  at increased pressure, leading to a stronger deceleration of the spray by mixing with ambient gas.  $\tilde{k}_{L|f}$  increases with pressure, which reflects a higher kinetic energy of liquid within the spray and confirms again the reinforced multiphase momentum transfer due to elevated pressure or  $M$  and  $We_G$  ( $M, We_G \propto p$ ). The progresses of  $\tilde{k}_{L|f}$  over  $\bar{f}$  are fitted by exponential functions  $\tilde{k}_{L|f}/k_{L,0} = a \cdot \exp(b \cdot \bar{f})$  for the range of  $0.005 < \bar{f} < 0.05$  and shown in Fig.12 by the dashed lines. The regression curves yield an almost constant factor in the exponent with  $b \approx -0.55$  and an increasing pre-exponential coefficients  $a$  with increased pressure. Note that Fig.12 does not present the energy spectrum in terms of the droplet size distribution, but it provides an estimation of liquid phase energy or velocity conditioned to the resolved liquid volume fraction.

In Fig.13, the time-averaged overall kinetic energy density of liquid has been evaluated from the ratio of the total liquid kinetic energy and volume within the spray zone:  $\bar{k}_{L,S} = (\int \bar{k}_L dV)/(\int \bar{f} dV)$  for  $0.005 < \bar{f} < 0.05$ , which increases monotonously with pressure. The solid line in Fig.13 denotes the fitting curve of simulated  $\bar{k}_{L,S}$  by a power function, with the fitting parameter indicated in the figure. The exponent of the power law fitting with 0.86 is close



to unity, denoting a quasi-linear growth of  $\bar{k}_{L,S}$  with  $p$ . The correlations of  $\bar{k}_{L,S}$  and  $\bar{k}_{L,S}$  in dependence of  $p$ ,  $M$  or  $We_G$  can be regarded as a first-order estimate of the multiphase momentum transfer for primary atomization of co-axial liquid jets and the subsequent spray dynamics. To do this, the kinetic energy or velocity of the liquid phase in the spray can be predicted based on given  $M$  or  $We_G$  ( $M, We_G \propto p$ ). In addition, the smaller the liquid volume fraction, the higher is the kinetic energy or speed of droplets. For the current setup it can be stated that the overall kinetic energy within the spray zone is roughly increased by a factor of approx.  $\bar{k}_{L,S}/k_{L,0} \approx 30 - 130$  for different pressures or  $M$  (see Fig.13), leading to a mean velocity of droplets in the spray of  $\bar{v}_{L,S}/v_{L,0} = \sqrt{\bar{k}_{L,S}/k_{L,0}} \approx 5 - 11$ .

In a previous work [44], the same numerical method has been used to simulate the primary atomization of a water jet and a glycerol/water mixture jet at  $GLR = 0.8$ , using the same pressure-adapted nozzles for  $p = 1, 2$  and 6 bar. Although the grid resolution used in [44] is coarse compared with the current work, the simulation results revealed qualitatively the same behaviour with regard to the effect of elevated pressure on the characteristics for primary breakup and liquid phase kinetic energy, as obtained in the present work.

## 5. Conclusion

Numerical simulations have been carried out to study the effect of elevated pressure on the primary atomization of high-viscous liquid jets from air-assisted, external mixing nozzles. A simplified nozzle configuration used by a real entrained flow gasification device has been applied in this work, where the pressure has been varied from 1 to 6 bar while keeping the gas-to-liquid mass flow ratio and momentum ratio constant. The main results are summarized below:

- In agreement with corresponding experiments [36], the simulations reveal a pulsating mode instability and disintegration of fibre-type liquid fragments at varied pressures due to the high gas-to-liquid momentum ratio.
- The mechanism for the breakup process has been confirmed to be triggered by a large concentric ring vortex with inwardly recirculating flows, which penetrates into the liquid core and tears off the intact liquid jet by dragging it from the tip and squeezing it at the base.
- The calculated exponent ( $b = -0.51$ ) from the power law fitting for the decay of the breakup length  $L_C$  with pressure shows a quantitatively good agreement with measured correlations of  $L_C$  from literature regarding the momentum flux ratio  $M$  and the Weber number  $We_G$ , even though water jets, atmospheric condition and different nozzles were applied in these works.
- The specific liquid kinetic energy  $k_L$  has been found to be increased at higher pressure, confirming a reinforced

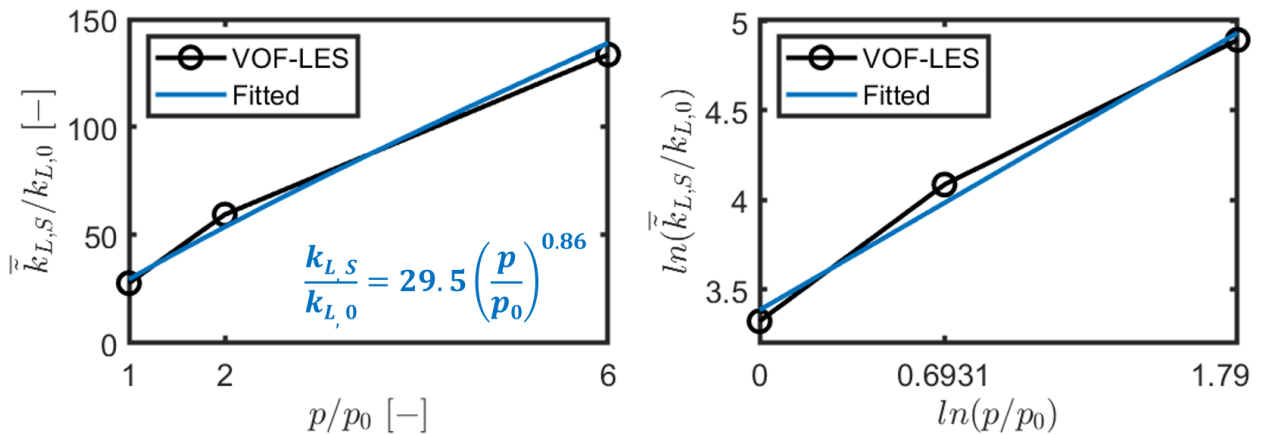


**Figure 13:** Correlation of overall liquid kinetic energy density in the spray zone with pressure. The calculated results from VOF-LES (circle) are fitted by a power law function, which are shown on the left with a linear scale and on the right with a double logarithmic scale.

multiphase momentum exchange. The increase of  $k_L$  with pressure is particularly noticeable in the high frequency range dominated by small-scale multiphase interactions.

- The volumetric kinetic energy density of liquid evaluated in the spray zone has been found to be higher at elevated pressure, which increases almost exponentially with decreasing liquid volume fractions.
- The same behaviour for primary breakup characteristics has been confirmed by simulations using a twice-refined grid. The finer grid reproduces however a better resolution of the secondary breakup process with smaller droplets.

The result reveals that the effect of elevated pressure on  $L_C$  is equivalent with that of increased  $M$  or  $We_G$ , which are linearly related to pressure ( $M, We_G \propto p$ ) for the current setup. VOF-LES applying under-resolved grid resolutions are able to reproduce dominant phenomena during primary atomization, further refined grids are however required for resolving a more realistic spray caused by secondary breakup. A first-order power law estimate for the liquid kinetic energy has been proposed, which may be used to assess multiphase momentum exchange and spray dynamics in dependence of increased pressure or  $M$  and  $We_G$ .

## Acknowledgments

The authors gratefully acknowledge the financial support by the Helmholtz Association of German Research Centers (HGF), within the research field Energy, Material and Resources, Topic 4 Gasification (34.14.02) and the computing time provided by the Steinbuch Centre for Computing (SCC) at the Karlsruhe Institute of Technology.

## References

- [1] A. Lefebvre, V. McDonell, *Atomization and sprays*, CRC press, 2017.
- [2] N. Ashgriz, *Handbook of atomization and sprays: theory and applications*, Springer Science & Business Media, 2011.
- [3] P. Marmottant, E. Villermaux, On spray formation, *J. Fluid Mech.* 498 (2004) 73–111.
- [4] C. Dumouchel, On the experimental investigation on primary atomization of liquid streams, *Exp Fluids* 45 (3) (2008) 371–422.
- [5] Z. Farago, N. Chigier, Parametric experiments on coaxial airblast jet atomization, in: *ASME 1990 International Gas Turbine and Aeroengine Congress and Exposition*, American Society of Mechanical Engineers, 1990, pp. V003T06A016–V003T06A016.
- [6] H. Eroglu, N. Chigier, Z. Farago, Coaxial atomizer liquid intact lengths, *Phys. Fluids A*. 3 (2) (1991) 303–308.
- [7] N. Chigier, Z. Farago, Morphological classification of disintegration of round liquid jets in a coaxial air stream, *At. Sprays* 2 (2) (1992).
- [8] R. Woodward, R. Burch, K. K. Kuo, F. B. Cheung, Correlation of intact-liquid core length for coaxial injectors, in: *Proceedings of ICLASS*, Vol. 94, 1994, pp. 105–112.
- [9] C. Engelbert, Y. Hardalupas, J. H. Whitelaw, Breakup phenomena in coaxial airblast atomizers, *Proc. Royal Soc. London A: Math Phys Eng Sci* 451 (1941) (1995) 189–229.
- [10] J. Lasheras, E. Villermaux, E. Hopfinger, Break-up and atomization of a round water jet by a high-speed annular air jet, *J. Fluid Mech.* 357 (1998) 351–379.
- [11] J. C. Lasheras, E. Hopfinger, Liquid jet instability and atomization in a coaxial gas stream, *Annu. Rev. Fluid Mech.* 32 (1) (2000) 275–308.
- [12] U. Shavit, Gas-liquid interaction in the liquid breakup region of twin-fluid atomization, *Exp Fluids* 31 (5) (2001) 550–557.
- [13] E. Porcheron, J. L. Carreau, D. Le Visage, F. Roger, Effect of injection gas density on coaxial liquid jet atomization, *At. Sprays* 12 (1-3) (2002).
- [14] W. Mayer, R. Branam, Atomization characteristics on the surface of a round liquid jet, *Exp Fluids* 36 (4) (2004) 528–539.
- [15] N. Chigier, *The future of atomization and sprays*, in: *Proceedings of ILASS-Europe*, 2005.
- [16] B. Leroux, O. Delabroy, F. Lacas, Experimental study of coaxial atomizers scaling. part i: dense core zone, *At. Sprays* 17 (5) (2007).
- [17] H. Zhao, H. Liu, J. Xu, W. Li, W. Cheng, Breakup and atomization of a round coal water slurry jet by an annular air jet, *Chem. Eng. Sci.* 78 (2012) 63–74.
- [18] X. Tian, H. Zhao, H. Liu, W. Li, J. Xu, Liquid entrainment behavior at the nozzle exit in coaxial gas–liquid jets, *Chem. Eng. Sci.* 107 (2014) 93–101.
- [19] A. Kumar, S. Sahu, Liquid jet breakup unsteadiness in a coaxial air-blast atomizer, *Int. J. Spray Combust. Dyn.* 10 (3) (2018) 211–230.
- [20] F. Xiao, M. Dianat, J. J. McGuirk, Les of turbulent liquid jet primary breakup in turbulent coaxial air flow, *Int. J. Multiph. Flow* 60 (2014) 103–118.
- [21] M. Gorokhovski, M. Herrmann, Modeling primary atomization, *Annu. Rev. Fluid Mech.* 40 (2008) 343–366.
- [22] J. Shinjo, A. Umemura, Simulation of liquid jet primary breakup: Dynamics of ligament and droplet formation, *Int. J. Multiph. Flow* 36 (7) (2010) 513–532.
- [23] A. Zandian, W. Sirignano, F. Hussain, Planar liquid jet: Early deformation and atomization cascades, *Phys. Fluids* 29 (2017) 062109.
- [24] V. Srinivasan, A. J. Salazar, K. Saito, Modeling the disintegration of modulated liquid jets using volume-of-fluid (vof) methodology, *Appl. Math. Model.* 35 (8) (2011) 3710–3730.
- [25] B. Duret, J. Reveillon, T. Menard, F. Demoulin, Improving primary atomization modeling through dns of two-phase flows, *Int. J. Multiph. Flow* 55 (2013) 130–137.

- [26] H. Grosshans, A. Movaghar, L. Cao, M. Oevermann, R.-Z. Szász, L. Fuchs, Sensitivity of vof simulations of the liquid jet breakup to physical and numerical parameters, *Comput Fluids* 136 (2016) 312–323.
- [27] T. Müller, A. Sängler, P. Habisreuther, T. Jakobs, D. Trimis, T. Kolb, N. Zarzalis, Simulation of the primary breakup of a high-viscosity liquid jet by a coaxial annular gas flow, *Int. J. Multiph. Flow* 87 (2016) 212–228.
- [28] M. Saeedipour, S. Pirker, S. Bozorgi, S. Schneiderbauer, An eulerian–lagrangian hybrid model for the coarse-grid simulation of turbulent liquid jet breakup, *Int. J. Multiph. Flow* 82 (2016) 17–26.
- [29] K. Warncke, S. Gepperth, B. Sauer, A. Sadiki, J. Janicka, R. Koch, H.-J. Bauer, Experimental and numerical investigation of the primary breakup of an airblasted liquid sheet, *Int. J. Multiph. Flow* 91 (2017) 208–224.
- [30] P. Beard, J.-M. Duclos, C. Habchi, G. Bruneaux, K. Mokaddem, T. Baritaud, Extension of lagrangian-eulerian spray modeling: Application to high pressure evaporating diesel sprays, *SAE transactions* (2000) 1417–1434.
- [31] R. Lebas, T. Menard, P.-A. Beau, A. Berlemont, F.-X. Demoulin, Numerical simulation of primary break-up and atomization: Dns and modelling study, *Int. J. Multiph. Flow* 35 (3) (2009) 247–260.
- [32] R. Gjesing, J. Hattel, U. Fritsching, Coupled atomization and spray modelling in the spray forming process using openfoam, *Eng. Appl. Comput. Fluid Mech.* 3 (4) (2009) 471–486.
- [33] Z. Zhou, G. Lu, B. Chen, Numerical study on the spray and thermal characteristics of r404a flashing spray using openfoam, *Int. J. Heat Mass Transf.* 117 (2018) 1312–1321.
- [34] T. Kolb, M. Aigner, R. Kneer, M. Mueller, R. Weber, N. Djordjevic, Tackling the challenges in modelling entrained-flow gasification of low-grade feedstock, *J. Energy Inst.* 89 (4) (2016) 485–503.
- [35] Bioliq, The bioliq process (2018).  
URL <https://www.bioliq.de/english/55.php>
- [36] S. Wachter, T. Jakobs, T. Kolb, Experimental investigation on the influence of system pressure on resulting spray quality and jet breakup applying pressure adapted twin-fluid nozzles, *Int. J. Multiph. Flow* 125 (2020).
- [37] OpenFOAM, The open source cfd toolbox (2018).  
URL <https://www.openfoam.com/releases/openfoam-v1806/>
- [38] A. Prosperetti, G. Tryggvason (Eds.), *Computational Methods for Multiphase Flow*, Cambridge University Press, Cambridge, 2007.
- [39] G. Yeoh, J. Tu, *Computational Techniques for Multiphase Flows*, Elsevier Science, 2009.
- [40] X.-S. Tian, H. Zhao, H. Liu, W. Li, J. Xu, Three-dimensional large eddy simulation of round liquid jet primary breakup in coaxial gas flow using the vof method, *Fuel Process. Technol.* 131 (2015) 396–402.
- [41] J. Fröhlich, *Large eddy simulation turbulenter Strömungen*, Vieweg+Teubner Verlag, 2007.
- [42] T. Müller, K. Kadel, P. Habisreuther, D. Trimis, N. Zarzalis, A. Sängler, T. Jakobs, T. Kolb, Influence of reactor pressure on the primary jet breakup of high-viscosity fuels: basic research for simulation-assisted design of low-grade fuel burner, in: *Proceedings of ASME Turbo Expo*, 2018, pp. GT2018–75950.
- [43] R. Henrik, *Computational fluid dynamics of dispersed two-phase flows at high phase fractions*, PhD thesis, Imperial College London, 2003.
- [44] T. Zhang, F. Müller, T. Zirwes, S. Wachter, T. Jakobs, P. Habisreuther, N. Zarzalis, T. Dimosthenis, T. Kolb, Numerical and experimental investigations of primary breakup of high-viscous fluid at elevated pressure, in: *Proceedings of ILASS-Europe*, 2019.
- [45] E. Berberović, N. P. van Hinsberg, S. Jakirlić, I. V. Roisman, C. Tropea, Drop impact onto a liquid layer of finite thickness: Dynamics of the cavity evolution, *Phys Rev E* 79 (3) (2009) 036306.
- [46] A. Sängler, T. Jakobs, N. Djordjevic, T. Kolb, Experimental investigation on the influence of ambient pressure on twin-fluid atomization of liquids with various viscosities, in: *International Conference for Liquid Atomization and Spray System (ICLASS)*, 2015, pp. 23–27.